

Comparison of Three Small-Signal Stability Analysis Methods for Grid-Following Inverter

Huang, Liang; Wu, Chao; Zhou, Dao; Blaabjerg, Frede

Published in:

2021 International Aegean Conference on Electrical Machines and Power Electronics (ACEMP) & 2021 International Conference on Optimization of Electrical and Electronic Equipment (OPTIM)

DOI (link to publication from Publisher):

[10.1109/OPTIM-ACEMP50812.2021.9590036](https://doi.org/10.1109/OPTIM-ACEMP50812.2021.9590036)

Publication date:

2021

Document Version

Accepted author manuscript, peer reviewed version

[Link to publication from Aalborg University](#)

Citation for published version (APA):

Huang, L., Wu, C., Zhou, D., & Blaabjerg, F. (2021). Comparison of Three Small-Signal Stability Analysis Methods for Grid-Following Inverter. In *2021 International Aegean Conference on Electrical Machines and Power Electronics (ACEMP) & 2021 International Conference on Optimization of Electrical and Electronic Equipment (OPTIM)* (pp. 34-41) <https://doi.org/10.1109/OPTIM-ACEMP50812.2021.9590036>

General rights

Copyright and moral rights for the publications made accessible in the public portal are retained by the authors and/or other copyright owners and it is a condition of accessing publications that users recognise and abide by the legal requirements associated with these rights.

- Users may download and print one copy of any publication from the public portal for the purpose of private study or research.
- You may not further distribute the material or use it for any profit-making activity or commercial gain
- You may freely distribute the URL identifying the publication in the public portal -

Take down policy

If you believe that this document breaches copyright please contact us at vbn@aub.aau.dk providing details, and we will remove access to the work immediately and investigate your claim.

Comparison of Three Small-Signal Stability Analysis Methods for Grid-Following Inverter

Liang Huang, Chao Wu, Dao Zhou, and Frede Blaabjerg

Department of Energy Technology

Aalborg University

Aalborg, Denmark

lihu@et.aau.dk, cwu@et.aau.dk, zda@et.aau.dk, fbl@et.aau.dk

Abstract—Conventional vector current control (VCC) based grid-following inverters suffer from stability issues under weak grid, which attracts a lot of attention in recent years. Small-signal linearized model is an effective tool to analyze the stability of such nonlinear systems. In this paper, three small-signal stability analysis methods are compared, which are the state-space method, impedance analysis method, and equivalent single-input single-output (SISO) stability analysis method. These three methods are based on the same primitive system but with different input-output relations. Through strict analysis, it is found that the three methods basically predict the same stability boundary. Finally, the advantages and disadvantages of three methods are summarized and compared.

Keywords—small-signal model, stability analysis, comparison, vector current control, grid following inverter

I. INTRODUCTION

As the penetration rate of wind generation increases, the power grid connected to renewable energy generation is weaker than before [1], due to the larger impedance of long-distance transmission line. This weak grid condition will cause severe voltage deviation at the point of common coupling (PCC) and some instability issues. Therefore, the study about the control stability of grid-connected inverters has become a hot topic [2]. At present, the classical phase-locked loop (PLL) based vector current control (VCC) scheme is still a mainstream control scheme in actual wind or solar photovoltaic generation systems. Therefore, this paper mainly focuses on the stability analysis of this control scheme.

To analyze the stability of this nonlinear system, small-signal linearized model is an effective tool. To the best knowledge of the authors, state-space method and impedance-based method are two widely used methods [3]. Each one has its own advantages and disadvantages.

The state-space method is versatile for any linearized system. Based on the state-space matrix, all the eigenvalues can be calculated for the stability analysis, so that the stability boundary of the system can be predicted accurately [4]. However, it needs a full knowledge of the control design of the system, which is often difficult to obtain and validate in practice [3]. Thus, it is only suitable for the white-box system.

Differently, the impedance model can be measured and validated directly without a full knowledge of the design details. Therefore, it can be used for a black-box system where all the parameters are unknown [5], [6]. Moreover, for a white-box system, the impedance model is also a good choice. Because each component can be represented by a transfer function and these transfer functions can be connected like the real control structure, so that the model can be visualized [4], [7]. Based on this visualized structure, impedance reshaping

methods can be found to enhance the stability [8], [9]. Furthermore, the generalized Nyquist criterion (GNC) is usually used for impedance model to analyze the stability.

Recently, an equivalent single-input single-output (SISO) stability analysis method is proposed in [10], which is very interesting. Because four elements in the two-by-two closed-loop transfer function matrix have the same denominator, they can be treated as one equivalent SISO transfer function. The same denominator can be considered as the characteristic expression so that the SISO stability analysis can be used. Thus, the stability margin can be found through Bode diagram, which is an important advantage of this method.

Additionally, since the modeling of the MIMO grid-following inverter system is complicated no matter which modeling method is chosen, it is hard to say if the stability analysis results are correct or not by only seeing the results of one method. Hence, a benefit of using three methods cooperatively is that stability analysis results of the three methods can be compared and verified one another. This is a major reason for introducing three stability analysis methods in this paper. Moreover, the main advantages and distinction of three methods are summarized and compared in the end of this paper. It is helpful for readers to know which method is preferred to use in different cases.

The rest of this paper is organized as follows. Section II introduces the time-domain and frequency-domain small-signal modeling process in detail. Section III compares three stability analysis methods and the results. The advantages and limitation of three methods are summarized. Then, the simulation results are presented in Section IV. Finally, this paper is concluded in Section V.

II. MOEDLING FOR GRID-FOLLOWING INVERTER SYSTEM

A. Configuration of Grid-Following Inverter

Fig. 1 shows schematic diagram of the classical VCC grid-following inverter connected to a weak grid. $V_c \angle \theta_c$ is the converter output voltage vector, $V_o \angle \theta_o$ is the output voltage vector at the PCC, and $V_g \angle \theta_g$ is the grid voltage vector. The voltages $v_{o(abc)}$ and the currents $i_{c(abc)}$ are three-phase instantaneous PCC voltages and the converter currents. The grid can be represented by a Thevenin equivalent impedance $Z_g = R_g + j\omega L_g$, where L_g and R_g are the equivalent grid inductance and resistance. The grid angular frequency ω is considered as a constant and equal to the nominal value ω_N . L_f and R_f are the output filter inductance and resistance. C_f is the output filter capacitance. To avoid low-frequency passive resonances on the grid side, the value of C_f is designed close to zero. The control diagram includes a d -axis and q -axis inner current control loop, an outer AC voltage magnitude control

loop, an outer active power control loop, and a phase-locked loop. The AC voltage magnitude reference is given 1 per unit (pu), so that it is equal to the nominal value. The definition of the short circuit ratio (SCR) can be found in [11]. A weak grid condition with $SCR < 3$ is used for analyses in this paper.

The control system is performed in the rotating $d-q$ frame, which is synchronized to the PCC voltage phase angle. Although the $d-q$ control frame is expected to be oriented to the PCC voltage phase angle θ_o , the phase angle θ_o is unknown. Hence, it is actually oriented to the PLL output angle θ_{pll} . These two angles have a small error in the dynamic state [7]. Thus, the control $d-q$ frame and the system $d-q$ frame are shown in Fig. 2. To be clear, the superscript ' $ctrl$ ' denotes the variables in the control $d-q$ frame. The symbol ' Δ ' denotes a small-signal perturbation of a variable, and the subscript ' 0 ' denotes a steady-state operating point in following sections.

B. Time-Domain Modeling

Firstly, the linearization of the differential equations are introduced. Based on these linearized differential equations, the small-signal state-space model can be established.

The differential equations of the L-C-L circuits in the system $d-q$ frame are given by (1)-(3).

$$\begin{cases} v_{od} - v_{gd} = L_g \frac{di_{od}}{dt} + R_g i_{od} - \omega L_g i_{oq} \\ v_{oq} - v_{gq} = L_g \frac{di_{oq}}{dt} + R_g i_{oq} + \omega L_g i_{od} \end{cases} \quad (1)$$

$$\begin{cases} i_{cd} - i_{od} = C_f \frac{dv_{od}}{dt} - \omega C_f v_{oq} \\ i_{cq} - i_{oq} = C_f \frac{dv_{oq}}{dt} + \omega C_f v_{od} \end{cases} \quad (2)$$

$$\begin{cases} v_{cd} - v_{od} = L_f \frac{di_{cd}}{dt} + R_f i_{cd} - \omega L_f i_{cq} \\ v_{cq} - v_{oq} = L_f \frac{di_{cq}}{dt} + R_f i_{cq} + \omega L_f i_{cd} \end{cases} \quad (3)$$

Since (1)-(3) are linear equations, they are same as the small-signal differential equations.

As shown in Fig.1 and Fig. 2, the Park and iPark transformations are used for the transformation between the system $d-q$ frame and the control $d-q$ frame. The equations of the coordinate transformations are given by (4).

$$\begin{cases} \begin{bmatrix} v_{od}^{ctrl} \\ v_{oq}^{ctrl} \end{bmatrix} = \begin{bmatrix} \cos(\theta_{pll} - \theta_o) & \sin(\theta_{pll} - \theta_o) \\ -\sin(\theta_{pll} - \theta_o) & \cos(\theta_{pll} - \theta_o) \end{bmatrix} \cdot \begin{bmatrix} v_{od} \\ v_{oq} \end{bmatrix} \\ \begin{bmatrix} i_{cd}^{ctrl} \\ i_{cq}^{ctrl} \end{bmatrix} = \begin{bmatrix} \cos(\theta_{pll} - \theta_o) & \sin(\theta_{pll} - \theta_o) \\ -\sin(\theta_{pll} - \theta_o) & \cos(\theta_{pll} - \theta_o) \end{bmatrix} \cdot \begin{bmatrix} i_{cd} \\ i_{cq} \end{bmatrix} \\ \begin{bmatrix} v_{cd} \\ v_{cq} \end{bmatrix} = \begin{bmatrix} \cos(\theta_{pll} - \theta_o) & -\sin(\theta_{pll} - \theta_o) \\ \sin(\theta_{pll} - \theta_o) & \cos(\theta_{pll} - \theta_o) \end{bmatrix} \cdot \begin{bmatrix} v_{cd}^{ctrl} \\ v_{cq}^{ctrl} \end{bmatrix} \end{cases} \quad (4)$$

The linearized small-signal equations of the coordinate transformations can be derived as:

$$\begin{cases} \Delta v_{od}^{ctrl} = \Delta v_{od} + v_{oq0} \cdot \Delta \theta_{pll} \\ \Delta v_{oq}^{ctrl} = \Delta v_{oq} - v_{od0} \cdot \Delta \theta_{pll} \end{cases} \quad (5)$$

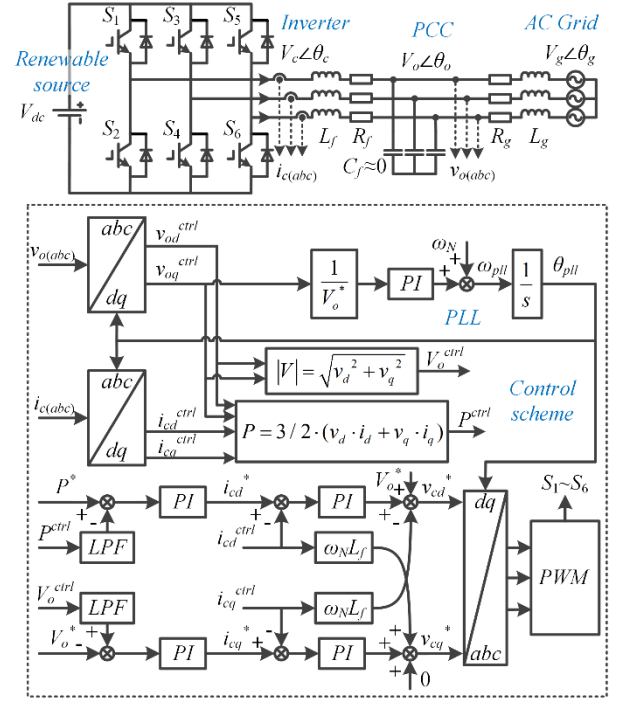


Fig. 1. Schematic diagram of classical vector current control grid-following inverter.

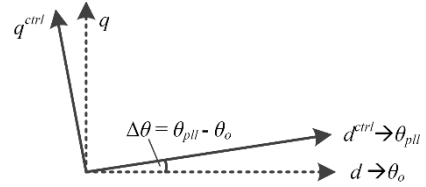


Fig. 2. Schematic diagram of voltage-oriented $d-q$ frames.

$$\begin{cases} \Delta i_{cd}^{ctrl} = \Delta i_{cd} + i_{cq0} \cdot \Delta \theta_{pll} \\ \Delta i_{cq}^{ctrl} = \Delta i_{cq} - i_{cd0} \cdot \Delta \theta_{pll} \end{cases} \quad (6)$$

$$\begin{cases} \Delta v_{cd} = \Delta v_{cd}^{ctrl} - v_{cq0} \cdot \Delta \theta_{pll} \\ \Delta v_{cq} = \Delta v_{cq}^{ctrl} + v_{cd0} \cdot \Delta \theta_{pll} \end{cases} \quad (7)$$

Moreover, the differential equations of the PLL are presented by (8).

$$\begin{cases} \frac{dInt_{pll}}{dt} = \frac{v_{oq}^{ctrl}}{V_o^*} \\ \frac{d\theta_{pll}}{dt} = \omega_{pll} = K_{p_pll} \cdot \frac{v_{oq}^{ctrl}}{V_o^*} + K_{i_pll} \cdot Int_{pll} + \omega_N \end{cases} \quad (8)$$

where Int_{pll} is the state variable of the integrator in the PLL.

The linearized small-signal equations of the PLL can be derived as:

$$\begin{cases} \frac{d\Delta Int_{pll}}{dt} = \frac{\Delta v_{oq}^{ctrl}}{V_o^*} \\ \frac{d\Delta \theta_{pll}}{dt} = \Delta \omega_{pll} = K_{p_pll} \cdot \frac{\Delta v_{oq}^{ctrl}}{V_o^*} + K_{i_pll} \cdot \Delta Int_{pll} \end{cases} \quad (9)$$

For the inner current control loop, the differential equations are given by (10) and (11).

$$\begin{cases} \frac{dInt_{id}}{dt} = i_{cd}^* - i_{cd}^{ctrl} \\ v_{cd}^* = K_{p_id}(i_{cd}^* - i_{cd}^{ctrl}) + K_{i_id} \cdot Int_{id} - \omega_N L_f i_{cq}^{ctrl} + V_o^* \end{cases} \quad (10)$$

$$\begin{cases} \frac{dInt_{iq}}{dt} = i_{cq}^* - i_{cq}^{ctrl} \\ v_{cq}^* = K_{p_iq}(i_{cq}^* - i_{cq}^{ctrl}) + K_{i_iq} \cdot Int_{iq} + \omega_N L_f i_{cd}^{ctrl} + 0 \end{cases} \quad (11)$$

where Int_{id} and Int_{iq} are the state variables of the integrator in the inner control loop.

Substituting “ $\omega_N = \omega$ ” into (10) and (11), then the linearized small-signal equations of the inner control loop can be derived as:

$$\begin{cases} \frac{d\Delta Int_{id}}{dt} = \Delta i_{cd}^* - \Delta i_{cd}^{ctrl} \\ \Delta v_{cd}^* = K_{p_id}(\Delta i_{cd}^* - \Delta i_{cd}^{ctrl}) + K_{i_id} \Delta Int_{id} - \omega L_f \Delta i_{cq}^{ctrl} \end{cases} \quad (12)$$

$$\begin{cases} \frac{d\Delta Int_{iq}}{dt} = \Delta i_{cq}^* - \Delta i_{cq}^{ctrl} \\ \Delta v_{cq}^* = K_{p_iq}(\Delta i_{cq}^* - \Delta i_{cq}^{ctrl}) + K_{i_iq} \Delta Int_{iq} + \omega L_f \Delta i_{cd}^{ctrl} \end{cases} \quad (13)$$

In addition, for the outer power and voltage control loops, the differential equations are given by (14) and (15).

$$\begin{cases} \frac{dInt_P}{dt} = P^* - P_{LPF}^{ctrl} \\ i_{cd}^* = K_{p_P}(P^* - P_{LPF}^{ctrl}) + K_{i_P} \cdot Int_P \end{cases} \quad (14)$$

$$\begin{cases} \frac{dInt_V}{dt} = V_o^* - V_{oLPF}^{ctrl} \\ i_{cq}^* = K_{p_V}(-1)(V_o^* - V_{oLPF}^{ctrl}) + K_{i_V}(-1) \cdot Int_V \end{cases} \quad (15)$$

where Int_P and Int_V are the state variables of the integrator in the outer control loops, P_{LPF}^{ctrl} and V_{oLPF}^{ctrl} are the active power feedback and AC voltage amplitude feedback after the low-pass filter (LPF).

Since (14) and (15) are linear equations, they are same as the small-signal differential equations.

Furthermore, the equations of the power and voltage magnitude calculation are provided by (16).

$$\begin{cases} P^{ctrl} = \frac{3}{2}(v_{od}^{ctrl} \cdot i_{cd}^{ctrl} + v_{oq}^{ctrl} \cdot i_{cq}^{ctrl}) \\ V_o^{ctrl} = \sqrt{(v_{od}^{ctrl})^2 + (v_{oq}^{ctrl})^2} \end{cases} \quad (16)$$

In the steady state, v_{od0}^{ctrl} is equal to V_o , and v_{oq0}^{ctrl} is equal to 0. Thus, the linearized small-signal equations can be derived as:

$$\begin{cases} \Delta P^{ctrl} = \frac{3}{2}(i_{cd0} \Delta v_{od}^{ctrl} + i_{cq0} \Delta v_{oq}^{ctrl} + V_o \Delta i_{cd}^{ctrl}) \\ \Delta V_o^{ctrl} = \Delta v_{od}^{ctrl} \end{cases} \quad (17)$$

Besides, the differential equations of the LPFs for power and voltage are given by (18).

$$\begin{cases} \frac{dP_{LPF}^{ctrl}}{dt} = \omega_{LPF} \cdot P^{ctrl} - \omega_{LPF} \cdot P_{LPF}^{ctrl} \\ \frac{dV_{oLPF}^{ctrl}}{dt} = \omega_{LPF} \cdot V_o^{ctrl} - \omega_{LPF} \cdot V_{oLPF}^{ctrl} \end{cases} \quad (18)$$

where ω_{LPF} is the cut-off angular frequency of the LPFs.

Since (18) are linear equations, they are same as the small-signal differential equations.

Assuming $\Delta v_{gd} = 0$ and $\Delta v_{gq} = 0$, thus, according to (1)-(3), (5)-(7), (9), (12)-(15), (17) and (18), the state-space expression can be derived as:

$$\Delta \dot{x}_{14 \times 1} = A_{14 \times 14} \cdot \Delta x_{14 \times 1} + B_{14 \times 2} \cdot \Delta u_{2 \times 1} \quad (19)$$

where $\Delta x_{14 \times 1} = [\Delta i_{od}, \Delta i_{oq}, \Delta v_{od}, \Delta v_{oq}, \Delta i_{cd}, \Delta i_{cq}, \Delta Int_{id}, \Delta Int_{iq}, \Delta Int_P, \Delta Int_V, \Delta \theta_{pll}, \Delta \theta_{pll}, \Delta P_{LPF}^{ctrl}, \Delta V_{oLPF}^{ctrl}]^T$, $\Delta u_{2 \times 1} = [\Delta P^*, \Delta V_o^*]^T$, $A_{14 \times 14}$ and $B_{14 \times 2}$ are shown in the Appendix.

Since the inputs ΔP^* and ΔV_o^* are usually given zero, (19) can be simplified as:

$$\Delta \dot{x}_{14 \times 1} = A_{14 \times 14} \cdot \Delta x_{14 \times 1} \quad (20)$$

It can be seen in (20), the stability of the system depends on the matrix $A_{14 \times 14}$. Given the steady-state operating point and all the control parameters, a constant matrix $A_{14 \times 14}$ is determined. Then, the eigenvalues of the matrix $A_{14 \times 14}$ can be solved to analyze the stability of the system. Thus, given different steady-state operating points, the stability boundary can be found according to the position of eigenvalues.

C. Frequency-Domain Modeling

According to the Laplace transformation, the time-domain model can also be expressed in the frequency domain.

Based on (1)-(3), the small-signal expressions of the L-C-L circuits in the system d - q frame can be derived as:

$$\begin{bmatrix} \Delta v_{od} \\ \Delta v_{oq} \end{bmatrix} - \begin{bmatrix} \Delta v_{gd} \\ \Delta v_{gq} \end{bmatrix} = \begin{bmatrix} sL_g + R_g & -\omega L_g \\ \omega L_g & sL_g + R_g \end{bmatrix} \cdot \begin{bmatrix} \Delta i_{od} \\ \Delta i_{oq} \end{bmatrix} \quad (21)$$

$$\begin{bmatrix} \Delta i_{cd} \\ \Delta i_{cq} \end{bmatrix} - \begin{bmatrix} \Delta i_{od} \\ \Delta i_{oq} \end{bmatrix} = \begin{bmatrix} sC_f & -\omega C_f \\ \omega C_f & sC_f \end{bmatrix} \cdot \begin{bmatrix} \Delta v_{od} \\ \Delta v_{oq} \end{bmatrix} \quad (22)$$

$$\begin{bmatrix} \Delta v_{cd} \\ \Delta v_{cq} \end{bmatrix} - \begin{bmatrix} \Delta v_{od} \\ \Delta v_{oq} \end{bmatrix} = \begin{bmatrix} sL_f + R_f & -\omega L_f \\ \omega L_f & sL_f + R_f \end{bmatrix} \cdot \begin{bmatrix} \Delta i_{cd} \\ \Delta i_{cq} \end{bmatrix} \quad (23)$$

Based on (5)-(7), the small-signal expressions of coordinate transformation between the system d - q frame and the control d - q frame can be rewritten as:

$$\begin{bmatrix} \Delta v_{od}^{ctrl} \\ \Delta v_{oq}^{ctrl} \end{bmatrix} = \begin{bmatrix} \Delta v_{od} \\ \Delta v_{oq} \end{bmatrix} + \begin{bmatrix} v_{oq0} \\ -v_{od0} \end{bmatrix} \cdot \Delta \theta_{pll} \quad (24)$$

$$\begin{bmatrix} \Delta i_{cd}^{ctrl} \\ \Delta i_{cq}^{ctrl} \end{bmatrix} = \begin{bmatrix} \Delta i_{cd} \\ \Delta i_{cq} \end{bmatrix} + \begin{bmatrix} i_{cq0} \\ -i_{cd0} \end{bmatrix} \cdot \Delta \theta_{pll} \quad (25)$$

$$\begin{bmatrix} \Delta v_{cd} \\ \Delta v_{cq} \end{bmatrix} = \begin{bmatrix} \Delta v_{cd}^{ctrl} \\ \Delta v_{cq}^{ctrl} \end{bmatrix} + \begin{bmatrix} -v_{cq0} \\ v_{cd0} \end{bmatrix} \cdot \Delta \theta_{pll} \quad (26)$$

$$Y(s) = \begin{bmatrix} Y_{dd}(s) & Y_{dq}(s) \\ Y_{qd}(s) & Y_{qq}(s) \end{bmatrix} \quad (38)$$

$$\begin{cases} Y_{dd}(s) = \frac{1}{sL_f + R_f} \frac{s}{s + \omega_i} + \frac{i_{cd0}}{V_o} \frac{\omega_p}{s} \frac{\omega_i}{s + \omega_i} \\ Y_{dq}(s) = \frac{i_{cq0}}{V_o} \frac{\omega_p}{s} \frac{\omega_i}{s + \omega_i} + \frac{(sL_f + R_f)\omega_i + sR_f}{(sL_f + R_f)(s + \omega_i)} G_{pll} \\ Y_{qd}(s) = \frac{-I_{max}}{V_o} \frac{\omega_v}{s} \frac{\omega_i}{s + \omega_i} \\ Y_{qq}(s) = \frac{1 - G_{pll}}{sL_f + R_f} \frac{s}{s + \omega_i} - \frac{i_{cd0}}{V_o} \frac{(sL_f + R_f)\omega_i + sR_f}{(sL_f + R_f)(s + \omega_i)} G_{pll} \end{cases} \quad (39)$$

D. Equivalent SISO model

The small-signal control diagram in Fig. 3 can also be used to calculate the closed-loop transfer function from the input $[\Delta P^*, \Delta V_o^*]^T$ to the output $[\Delta i_{cd}, \Delta i_{cq}]^T$, namely, $[\Delta i_{cd}, \Delta i_{cq}]^T = W_{cl}(s) \cdot [\Delta P^*, \Delta V_o^*]^T$. The closed-loop transfer function matrix $W_{cl}(s)$ is given in (40).

$$W_{cl}(s) = \begin{bmatrix} \frac{D(s) \cdot E(s)}{A(s) \cdot D(s) - B(s) \cdot C(s)} & \frac{-B(s) \cdot E(s)}{A(s) \cdot D(s) - B(s) \cdot C(s)} \\ \frac{-C(s) \cdot F(s)}{A(s) \cdot D(s) - B(s) \cdot C(s)} & \frac{A(s) \cdot F(s)}{A(s) \cdot D(s) - B(s) \cdot C(s)} \end{bmatrix} \quad (40)$$

where $A(s)$, $B(s)$, $C(s)$, $D(s)$, $E(s)$ and $F(s)$ are the multinomial about “ s ”, and they are shown in the Appendix.

As shown in (40), although the four elements are four SISO transfer functions, they have the same denominator, so that they can be treated as one equivalent SISO transfer function. The same characteristic expression “ $A(s)D(s) - B(s)C(s)$ ” can be used to analyze the stability.

III. STABILITY ANALYSIS RESULTS AND COMPARISON

Based on the parameters of a 380V-30kW grid-following inverter simulation platform (the parameters are listed in Table I), the results of three stability analysis methods can be compared. For example, given two different steady-state operating points, stability analysis results of three methods are shown in Figs. 4-6 respectively. Fig. 4 shows the eigenvalue loci of matrix $A_{14 \times 14}$ in (20). Fig. 5 shows the generalized Nyquist diagram of the matrix $Y(s) \cdot Z_g(s)$ based on (37)-(39). And Fig. 6 shows the Nyquist diagram of the equivalent open-loop transfer function “ $A(s)D(s) - B(s)C(s) - 1$ ” of SISO model.

It can be seen that the system is stable at 0.4 pu steady-state operating point but unstable at 0.6 pu steady-state operating point. So the stability boundary is between 0.4 pu and 0.6 pu. Further, given different steady-state operating points, the stability boundary can be found, which is 0.55 pu. Similarly, the stability boundary of the system when SCR is 2 and 3 can also be found. Thus, three stability boundaries of the system predicted by aforementioned three methods can also be found, which are shown in Fig. 7. It can be seen that three stability boundaries are very close.

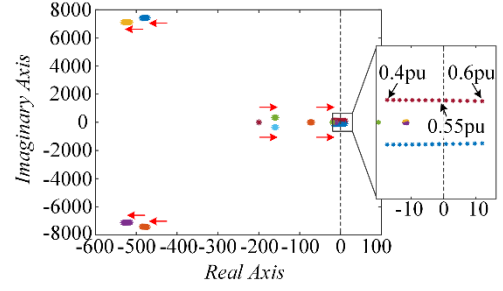


Fig. 4. Eigenvalues diagram by using state-space model. (Steady-state power point is changed from 0.4 pu to 0.6 pu)

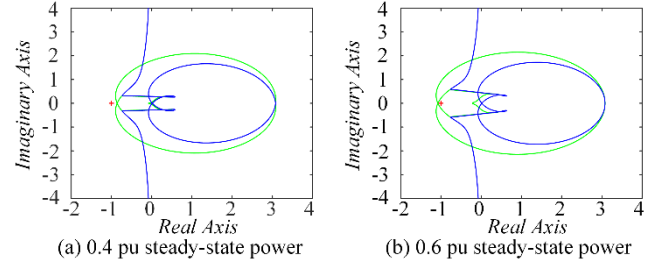


Fig. 5. Generalized Nyquist diagram by using impedance model.

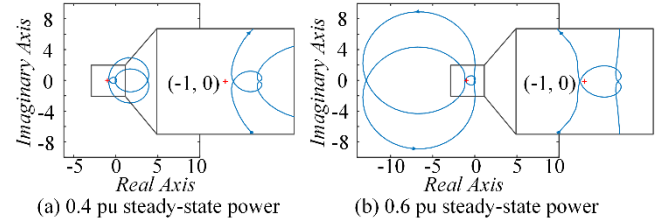


Fig. 6. Nyquist diagram by using equivalent SISO model.

TABLE I. PARAMETERS OF GRID-FOLLOWING INVERTER SYSTEM	
Parameters	Values
Grid phase voltage (peak value), V_g	311 V
Grid frequency, f_g	50 Hz
Rated power of inverter, S_N	30 kVA
Maximum current of inverter (peak value), I_{max}	64.3 A
DC-link voltage, V_{dc}	700 V
Output filter inductor, L_f	5 mH
Output filter capacitor, C_f	5 μ F
R/X ratio of grid impedance, R_g/X_g	0.01
Short circuit ratio, SCR	1
Grid inductor, L_g	15.3 mH
Grid resistor, R_g	0.048 Ω
Switching/sampling frequency, f_s	10 kHz
Designed current-loop bandwidth, ω_i	1000 rad/s
Designed AC voltage-loop bandwidth, ω_v	50 rad/s
Designed power-loop bandwidth, ω_p	10 rad/s
Cut-off angular frequency of LPF, ω_{LPF}	200 rad/s
Damping ratio of PLL, ζ	1
Natural angular frequency of PLL, ω_n	200 rad/s

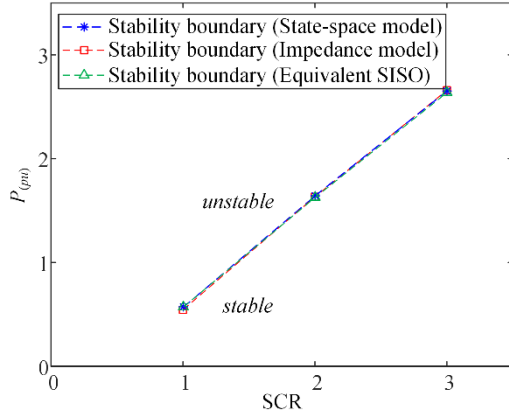


Fig. 7. Comparison of stability boundaries predicted by three small-signal models under different grid strengths.

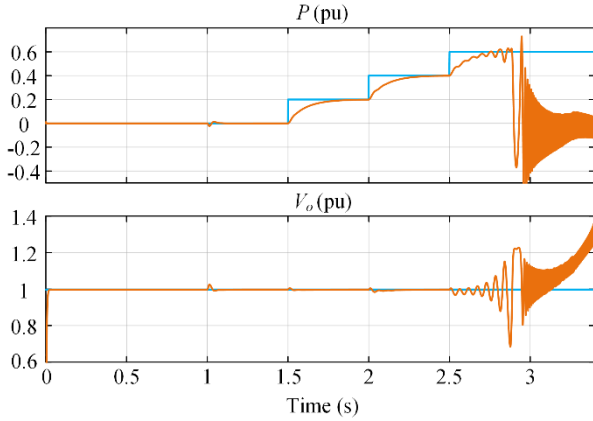


Fig. 8. Simulation results of the active power and PCC voltage magnitude with SCR = 1.

TABLE II. DIFFERENCE OF THREE STABILITY ANALYSIS METHODS

Methods	State-space	Impedance	SISO
Applicable range (for white-box system)	Wide	Medium [13]	Narrow [10]
Availability for black-box system	No	Yes [5], [6]	No
Visualization	Medium	High [3], [9]	Low
Scalability (for multi-converters system)	High [15]	High [16]	Medium
Difficulty about seeking stability margin	Medium	Medium	Easy

Although the three small-signal analysis methods are basically equivalent to predict the stability boundary, it is important to know the difference among them. The main advantages and disadvantages of three methods are compared in Table II. Further explanations are listed as below:

- 1) **Applicable range (for white-box system):** If all the design details are known, the state-space method is suitable for any linearized system. However, the impedance model has a precondition, which is the equivalent voltage source and current source must be stable [13]. If this precondition is not satisfied, the GNC results for impedance model are not correct. For the SISO model, it is only suitable for 2-dimensional system. When the three-phase voltages are

asymmetric, the system has 3 dimensions. In this case, the SISO model cannot be used [10].

- 2) **Availability for black-box system:** If all the design details are unknown, only the impedance model can be used, because the impedance can be measured through frequency scan methods [5], [6].
- 3) **Visualization:** For the impedance model, an equivalent gray-box structure can be established by connecting each component [3], which is helpful to find the major destabilizing factors caused by the PLL and improved control strategies to enhance the stability [9], [14].
- 4) **Scalability (for multi-converters system):** Both state-space model and impedance model can be used for multiple converters systems. The system can be divided into a few subsystems so that component connection method (CCM) can be used to study the stability of the whole systems [15], [16]. However, the SISO model has challenges to study a more complicated system.
- 5) **Difficulty about seeking stability margin:** Stability margin is an important performance index to evaluate the stability of the system. For SISO model, it is easy to find the stability margin on the Bode diagram. However, for the MIMO methods, it is not easy to do that.

IV. SIMULATION VERIFICATION

In order to verify the effectiveness of the theoretical analysis above, a time-domain simulation model of 30kW grid-connected inverter is built in Matlab/Simulink. The system and control parameters are shown in Table I, which are the same as the parameters used in small-signal stability analysis. To avoid the influence of high-frequency harmonics, the average model the inverter is used. The simulation results are shown in Fig. 8. It can be seen that when the power is increased to 0.4 pu, the system is still stable. However, when the power is increased to 0.6 pu, the system becomes unstable. Both the power and the PCC voltage magnitude are out of control. These simulation results agree well with the stability analysis results in Fig. 6.

V. CONCLUSION

Three small-signal stability analysis methods of the grid-following inverter are compared in this paper. Through exhaustive mathematical analysis, it is revealed that these three methods basically predict the same stability boundary. Further, the difference of three methods are compared, so that the advantages and disadvantages of each method are clear to see. Because the impedance model has advantages for both black-box and white-box systems, it could be the first choice when studying the small-signal stability of grid-following inverters. However, judging the stability of the system by watching the generalized Nyquist diagram is a challenge, because sometimes it is hard to see if all the Nyquist curves encircle the point $(-1, j0)$. Therefore, how to judge the stability automatically by computer according to the generalized Nyquist diagram is an interesting topic to study further.

Moreover, the state-space model can be used to check the correctness of the stability analysis results predicted by the impedance model. It is easy to judge the stability based on the positions of the eigenvalues. Besides, the equivalent SISO model can be used to analyze the stability margin quantitatively on the Bode diagram. Thus, three methods can be used cooperatively based on the study in this paper.

APPENDIX

$$A_{14 \times 14} = \begin{bmatrix} \frac{-R_g}{L_g} & \omega & \frac{1}{L_g} & 0 & 0 & 0 & 0 & 0 & 0 & 0 & 0 & 0 & 0 & 0 \\ -\omega & \frac{-R_g}{L_g} & 0 & \frac{1}{L_g} & 0 & 0 & 0 & 0 & 0 & 0 & 0 & 0 & 0 & 0 \\ \frac{-1}{C_f} & 0 & 0 & \omega & \frac{1}{C_f} & 0 & 0 & 0 & 0 & 0 & 0 & 0 & 0 & 0 \\ 0 & \frac{-1}{C_f} & -\omega & 0 & 0 & \frac{1}{C_f} & 0 & 0 & 0 & 0 & 0 & 0 & 0 & 0 \\ 0 & 0 & \frac{-1}{L_f} & 0 & \frac{R_f + K_{p_id}}{-L_f} & 0 & \frac{K_{p_id}}{L_f} & 0 & \frac{K_{p_id}K_{i_P}}{L_f} & 0 & 0 & A_{12,5} & A_{13,5} & 0 \\ 0 & 0 & 0 & \frac{-1}{L_f} & 0 & \frac{R_f + K_{p_iq}}{-L_f} & 0 & \frac{K_{p_iq}}{L_f} & 0 & \frac{K_{p_iq}K_{i_V}}{-L_f} & 0 & A_{12,6} & 0 & A_{14,6} \\ 0 & 0 & 0 & 0 & -1 & 0 & 0 & 0 & K_{i_P} & 0 & 0 & -i_{cq0} & -K_{p_P} & 0 \\ 0 & 0 & 0 & 0 & 0 & -1 & 0 & 0 & 0 & -K_{i_V} & 0 & i_{cd0} & 0 & K_{p_V} \\ 0 & 0 & 0 & 0 & 0 & 0 & 0 & 0 & 0 & 0 & 0 & 0 & -1 & 0 \\ 0 & 0 & 0 & 0 & 0 & 0 & 0 & 0 & 0 & 0 & 0 & 0 & 0 & -1 \\ 0 & 0 & 0 & \frac{1}{V_o} & 0 & 0 & 0 & 0 & 0 & 0 & 0 & -1 & 0 & 0 \\ 0 & 0 & 0 & \frac{K_{p_pll}}{V_o} & 0 & 0 & 0 & 0 & 0 & 0 & K_{i_pll} & -K_{p_pll} & 0 & 0 \\ 0 & 0 & \frac{3}{2}i_{cd0} \cdot \omega_{LPF} & \frac{3}{2}i_{cq0} \cdot \omega_{LPF} & \frac{3}{2}v_{od0} \cdot \omega_{LPF} & 0 & 0 & 0 & 0 & 0 & 0 & 0 & -\omega_{LPF} & 0 \\ 0 & 0 & \omega_{LPF} & 0 & 0 & 0 & 0 & 0 & 0 & 0 & 0 & 0 & 0 & -\omega_{LPF} \end{bmatrix} \quad (A1)$$

where, $A_{12,5} = (\omega L_f i_{cd0} - K_{p_id} i_{cq0} - v_{cd0}) / L_f$, $A_{12,6} = (\omega L_f i_{cq0} + K_{p_iq} i_{cd0} + v_{cd0}) / L_f$, $A_{13,5} = -K_{p_id} K_{p_P} / L_f$, and $A_{14,6} = K_{p_iq} K_{p_V} / L_f$.

$$B_{14 \times 2} = \begin{bmatrix} 0 & 0 & 0 & 0 & \frac{K_{p_id} K_{p_P}}{L_f} & 0 & K_{p_P} & 0 & 1 & 0 & 0 & 0 & 0 & 0 \\ 0 & 0 & 0 & 0 & 0 & \frac{K_{p_iq} K_{p_V}}{L_f} & 0 & -K_{p_V} & 0 & 1 & 0 & 0 & 0 & 0 \end{bmatrix}^T \quad (A2)$$

$$\begin{cases} A(s) = \{s\omega_i(sL_f + R_f) + s^2(sL_f + R_f + sL_g + R_g) + \omega_p\omega_i(sL_f + R_f) \cdot [1 + (sL_g + R_g)i_{cd0}/V_o + \omega L_g i_{cq0}/V_o]\} \\ \cdot (s^2 + 2\zeta\omega_n s + \omega_n^2) + s(\omega L_g) \cdot [\omega_i(sL_f + R_f) + sR_f] \cdot i_{cq0}/V_o \cdot (2\zeta\omega_n s + \omega_n^2) \\ B(s) = \{-s^2\omega L_g + \omega_p\omega_i(sL_f + R_f) \cdot [(sL_g + R_g) \cdot i_{cq0}/V_o - \omega L_g i_{cd0}/V_o]\} \cdot (s^2 + 2\zeta\omega_n s + \omega_n^2) \\ + s(sL_g + R_g) \cdot [\omega_i(sL_f + R_f) + sR_f] \cdot i_{cq0}/V_o \cdot (2\zeta\omega_n s + \omega_n^2) \\ C(s) = [s^2\omega L_g - \omega_v\omega_i(sL_f + R_f)(sL_g + R_g) \cdot I_{max}/V_o] \cdot (s^2 + 2\zeta\omega_n s + \omega_n^2) \\ - s(\omega L_g) \cdot \{s + [\omega_i(sL_f + R_f) + sR_f] \cdot i_{cd0}/V_o\} \cdot (2\zeta\omega_n s + \omega_n^2) \\ D(s) = [s\omega_c(sL_f + R_f) + s^2(sL_f + R_f + sL_g + R_g) + \omega_v\omega_i(sL_f + R_f)\omega L_g \cdot I_{max}/V_o] \cdot (s^2 + 2\zeta\omega_n s + \omega_n^2) \\ - s(sL_g + R_g) \cdot \{s + [\omega_i(sL_f + R_f) + sR_f] \cdot i_{cd0}/V_o\} \cdot (2\zeta\omega_n s + \omega_n^2) \\ E(s) = (s^2 + 2\zeta\omega_n s + \omega_n^2) \cdot (sK_{p_id} + K_{i_id}) \cdot (sK_{p_P} + K_{i_P}) \\ F(s) = -(s^2 + 2\zeta\omega_n s + \omega_n^2) \cdot (sK_{p_iq} + K_{i_iq}) \cdot (sK_{p_V} + K_{i_V}) \end{cases} \quad (A3)$$

REFERENCES

- [1] F. Blaabjerg, Y. Yang, D. Yang and X. Wang, "Distributed power-generation systems and protection," *Proc. IEEE*, vol. 105, no. 7, pp. 1311-1331, Jul. 2017.
- [2] X. Wang and F. Blaabjerg, "Harmonic stability in power electronic-based power systems: concept, modeling, and analysis," *IEEE Trans. Smart Grid*, vol. 10, no. 3, pp. 2858-2870, May 2019.
- [3] Y. Li, Y. Gu, Y. Zhu, A. Junyent-Ferré, X. Xiang and T. C. Green, "Impedance circuit model of grid-forming inverter: visualizing control algorithms as circuit elements," *IEEE Trans. Power Electron.*, vol. 36, no. 3, pp. 3377-3395, Mar. 2021.
- [4] J. A. Suul, S. D'Arco, P. Rodriguez, and M. Molinas, "Impedance-compensated grid synchronization for extending the stability range of weak grids with voltage source converters," *IET Gen., Trans. Distr.*, vol. 10, no. 6, pp. 1315-1326, Apr. 2016.
- [5] B. Wen, D. Boroyevich, R. Burgos, P. Mattavelli and Z. Shen, "Small-signal stability analysis of three-phase AC systems in the presence of constant power loads based on measured d-q frame impedances," *IEEE Trans. Power Electron.*, vol. 30, no. 10, pp. 5952-5963, Oct. 2015.
- [6] Y. Liao and X. Wang, "Stationary-frame complex-valued frequency-domain modeling of three-phase power converters," *IEEE J. Emerg. Sel. Top. Power Electron.*, vol. 8, no. 2, pp. 1922-1933, Jun. 2020.
- [7] B. Wen, D. Boroyevich, R. Burgos, P. Mattavelli and Z. Shen, "Analysis of D-Q small-signal impedance of grid-tied inverters," *IEEE Trans. Power Electron.*, vol. 31, no. 1, pp. 675-687, Jan. 2016.
- [8] D. Yang, X. Wang, F. Liu, K. Xin, Y. Liu and F. Blaabjerg, "Symmetrical PLL for SISO impedance modeling and enhanced stability in weak grids," *IEEE Trans. Power Electron.*, vol. 35, no. 2, pp. 1473-1483, Feb. 2020.
- [9] J. Fang, X. Li, H. Li and Y. Tang, "Stability improvement for three-phase grid-connected converters through impedance reshaping in quadrature-axis," *IEEE Trans. Power Electron.*, vol. 33, no. 10, pp. 8365-8375, Oct. 2018.
- [10] H. Zhang, X. Wang, L. Harnefors, H. Gong, J. Hasler and H. Nee, "SISO transfer functions for stability analysis of grid-connected voltage-source converters," *IEEE Trans. Ind. Appl.*, vol. 55, no. 3, pp. 2931-2941, May-June 2019.
- [11] L. Huang, C. Wu, D. Zhou, and F. Blaabjerg, "Impact of grid strength and impedance characteristics on the maximum power transfer capability of grid-connected inverters," *Appl. Sci.*, vol. 11, no. 9, pp. 4288, May 2021.
- [12] J. F. Morris, K. H. Ahmed and A. Egea-Alvarez, "Analysis of controller bandwidth interactions for vector-controlled VSC connected to very weak AC grids," *IEEE J. Emerg. Sel. Top. Power Electron. (Early Access)*, Oct. 2020.
- [13] J. Sun, "Impedance-based stability criterion for grid-connected inverters," *IEEE Trans. Power Electron.*, vol. 26, no. 11, pp. 3075-3078, Nov. 2011.
- [14] L. Huang, C. Wu, D. Zhou, and F. Blaabjerg, "A simple impedance reshaping method for stability enhancement of grid-following inverter under weak grid," *IEEE 12th Int. Symp. Power Electron. Distr. Gen. (PEDG)*, 2021, in press.
- [15] R. Rosso, S. Engelken and M. Liserre, "Analysis of the parallel operation between synchronverters and PLL-based converters," *IEEE Energy Conv. Cong. Expos. (ECCE)*, 2019, pp. 2583-2590.
- [16] R. Rosso, G. Buticchi, M. Liserre, Z. Zou and S. Engelken, "Stability analysis of synchronization of parallel power converters," *IECON 43rd Ann. Conf. IEEE Ind. Electron. Soc.*, 2017, pp. 440-445.